

Long-Term Photometric Consistent Novel View Synthesis with Diffusion Models

Jason J. Yu^{1,2}, Fereshteh Forghani¹, Konstantinos G. Derpanis^{1,2}, Marcus A. Brubaker^{1,2}

¹York University, ²Vector Institute for AI

{jjyu, forghani, kostas, marcus.brubaker}@yorku.ca



Figure 1: Our model allows us to sample multiple plausible views over a camera trajectory, given a single source view. Here, we show two samples (middle and right) of a sequence using the three source views (left). Our method is able to maintain consistency between observed regions, while plausibly extrapolating unseen regions. Notice that the final frames reveal regions that are largely unseen in the source view, and show different plausible appearances in each sample.

Abstract

Novel view synthesis from a single input image is a challenging task, where the goal is to generate a new view of a scene from a desired camera pose that may be separated by a large motion. The highly uncertain nature of this synthesis task due to unobserved elements within the scene (i.e., occlusion) and outside the field-of-view makes the use of generative models appealing to capture the variety of possible outputs. In this paper, we propose a novel generative model which is capable of producing a sequence of photorealistic images consistent with a specified camera trajectory, and a single starting image. Our approach is centred on an autoregressive conditional diffusion-based model capable of interpolating visible scene elements, and extrapolating unobserved regions in a view, in a geometrically consistent manner. Conditioning is limited to an image capturing a single camera view and the (relative) pose of the new

camera view. To measure the consistency over a sequence of generated views, we introduce a new metric, the thresholded symmetric epipolar distance (TSED), to measure the number of consistent frame pairs in a sequence. While previous methods have been shown to produce high quality images and consistent semantics across pairs of views, we show empirically with our metric that they are often inconsistent with the desired camera poses. In contrast, we demonstrate that our method produces both photorealistic and view-consistent imagery. Additional material is available on our project page: <https://yorkucvil.github.io/Photoconsistent-NVS/>.

1. Introduction

Novel view synthesis (NVS) approaches are generally tasked with generating new scene views, given a set of existing views. NVS has a long history in computer vision [4, 16, 1] and has recently seen a resurgence of interest with

the advent of NeRFs [21, 41, 36]. Most current approaches to NVS (*e.g.*, NeRFs) focus on problem settings where generated views remain close to the input and whose content is largely visible from some subset of the given views. This restricted setting makes these methods amenable to direct supervision. In contrast, we consider a more extreme case, where a single view is given as input, and the goal is to generate plausible image sequence continuations from a trajectory of provided camera views. By plausible, we mean that visible portions of the scene should evolve in a 3D consistent fashion, while previously unseen elements (*i.e.*, regions occluded or outside of the camera field-of-view) should appear harmonious with the scene. Moreover, regions not visible in the input view are generally highly uncertain; so, there are a variety of plausible continuations that are valid.

To address this challenge, we propose a novel NVS method based on denoising diffusion models [10] to sample multiple, consistent novel views. We condition the diffusion model on both the given view and a geometrically informed representation of the relative camera settings of both the given and target views. The resulting model is able to produce multiple plausible novel views by simply generating new samples from the model. Further, while the model is trained to generate a single novel view conditioned on an existing view and a target camera pose, we demonstrate that this model can be successfully used to generate a sequence of plausible views, including final views with little or no overlap with the starting view. Fig. 1 shows the outputs of our model for several different starting views.

Existing NVS techniques have been evaluated primarily in terms of generated image quality (*e.g.*, with Fréchet Inception Distance (FID) [9]) but have generally ignored measuring consistency with the camera poses. Based on the epipolar geometry defined by relative camera poses [8], we introduce a new metric which directly evaluates the geometric consistency of generated views independently from the quality of generated imagery. The proposed metric does not require any knowledge of scene geometry, making it widely applicable even on purely generated images. We evaluate the proposed method on both real and synthetic datasets in terms of both generated image quality and geometric consistency. Further, previous work evaluates performance based on ground truth camera trajectories. Here, we also evaluate the generalization ability of extant models and our own by generating sequences based on novel trajectories (*i.e.*, trajectories that differ significantly from those in the training data).

2. Related Work

NVS has been long studied in computer vision (*e.g.*, [4, 16, 1]), and a full review is out of scope for this paper. NVS methods can largely be categorized as those which focus on *view interpolation*, where generated views remain

close to the given views, and *view extrapolation*, where the generated field-of-view may contain large amounts of novel content. Many current view interpolation methods are based on NeRFs [21, 41], which leverage neural-network representations of radiance fields fit to the observed images. Others attempt to directly regress novel views [31] from a set-encoded representation of the given views. Alternatively, if depth information is available, images can be back-projected into 3D, and missing regions inpainted [15]. We focus on view extrapolation NVS where significant portions of the generated images are not visible in the inputs.

View extrapolation methods are largely built on probabilistic approaches to capture the high degree of uncertainty. GAUDI [2] learns a latent variable model of entire 3D scenes represented as a neural radiance field and then estimates the latents given observed images. However, the estimated scene representation often has a limited spatial extent, which is in contrast to image-to-image methods [18] which may extend indefinitely. GeoGPT [28] used an autoregressive likelihood model to sample novel views conditioned on a single source view. In contrast, we use a latent diffusion model [23, 27], and investigate sequential view generation. LookOut [25] extends GeoGPT [28] to generate sequences of views along a trajectory, while conditioning on up to two previous views. To enforce consistency LookOut requires a post-processing step that uses generated outputs as additional conditioning. In contrast, our model is conditioned on a single view, and does not require additional post-processing to achieve consistency. A closely related method [38] also formulates a diffusion model for NVS, however, it was only applied to simple scenes (*i.e.*, isolated objects) with constrained camera poses. Here, we consider view extrapolation on real indoor scenes with complex geometry, and without constraints on camera motion.

Conditional generative models are a common approach for complex tasks such as view synthesis [28, 25], image editing [20], and video prediction [17]. Recent years has seen significant progress in generative modelling [14, 32, 10, 6, 5] with diffusion models [27, 33, 10] becoming successful in many tasks, *e.g.*, text-to-image generation [27, 30], and video modeling [12]. In our problem, we utilize latent diffusion models [23, 27], which first compress high dimensional images with an autoencoder and discourage the diffusion model from expending capacity on modeling imperceptible details. The resulting model is more efficient, and uses less computation during training and inference.

3. Technical Approach

3.1. Background: Diffusion Models

A full review of diffusion models is beyond the scope of this work. Here, we provide a brief introduction to ground

the following developments but refer interested readers to a recent detailed review [39]. Diffusion models are a class of generative models where sampling is performed by reversing a stochastic diffusion process [10, 33]. The forward process is fixed, typically Gaussian, and discretized into T timesteps which are defined recursively as

$$q(\mathbf{x}_t|\mathbf{x}_{t-1}) = \mathcal{N}(\mathbf{x}_t; \sqrt{1 - \beta_t}\mathbf{x}_{t-1}, \beta_t\mathbf{I}), \quad (1)$$

where \mathbf{x}_0 is a sample from the data distribution of interest, $q(\mathbf{x}_0)$, \mathbf{I} is an identity matrix, and β_t is dependent on the particular forward process used. Repeatedly applying Eq. 1 adds Gaussian noise with \mathbf{x}_T approximately normally distributed for large values of T . The reverse process is parameterized by θ and takes the form of a parameterized Gaussian:

$$p_\theta(\mathbf{x}_{t-1}|\mathbf{x}_t) = \mathcal{N}(\mathbf{x}_{t-1}; \mu_\theta(\mathbf{x}_t, t), \Sigma_\theta(\mathbf{x}_t, t)), \quad (2)$$

where the variance, $\Sigma_\theta(\mathbf{x}_{t-1}, t)$, is generally set as constant. Here, \mathbf{x}_{t-1} is expressed using $\epsilon_\theta(\mathbf{x}_t, t)$ which is implemented as a neural network:

$$\mathbf{x}_{t-1} = \frac{1}{\sqrt{\alpha_t}} \left(\mathbf{x}_t - \frac{1 - \alpha_t}{\sqrt{1 - \bar{\alpha}_t}} \epsilon_\theta(\mathbf{x}_t, t) \right) + \sigma_t \mathbf{z}_t, \quad (3)$$

where $\alpha_t = 1 - \beta_t$, $\bar{\alpha}_t = \prod_{s=1}^t \alpha_s$, and $\mathbf{z}_t \sim \mathcal{N}(0, I)$. The function $\epsilon_\theta(\mathbf{x}_t, t)$ is referred to as the score function and can be interpreted as a noise estimator which can be used to denoise \mathbf{x}_t to produce \mathbf{x}_{t-1} . Training is performed using denoising score matching [37]:

$$\mathcal{L} = \mathbb{E}_{\mathbf{x}_0, \epsilon} [\|\epsilon - \epsilon_\theta(\sqrt{\alpha_t}\mathbf{x}_0 + \sqrt{1 - \bar{\alpha}_t}\epsilon, t)\|^2]. \quad (4)$$

Samples can be drawn from the model by initializing \mathbf{x}_T with Gaussian noise, and iteratively applying the learned reverse process given in Equation 2. The model can be made conditional by providing additional inputs to the score function, $\epsilon_\theta(\mathbf{x}_t, t)$. Due to the redundant and high dimensional nature of images, it is beneficial to first reduce their dimensionality. There are several ways to approach the dimensionality reduction task [7, 11, 23, 27]. Here, we use a latent diffusion model [23, 27] that first transforms an image, \mathbf{x} , into a latent representation, \mathbf{z} , with a learned autoencoder, $\mathbf{z} = \mathbf{E}(\mathbf{x})$. The diffusion model is then learned in the latent space, \mathbf{z} , and images can be recovered by using the corresponding decoder, $\mathbf{x} = \mathbf{D}(\mathbf{z})$. Critically for us, the learned latent representation can maintain the spatial structure of the image, *e.g.*, through the use of a convolutional encoder architecture.

3.2. Novel View Synthesis with Diffusion Models

We now describe how we use a diffusion model to sample multiple plausible views in novel view synthesis. A conditioning image, \mathbf{x}_1 , is first mapped into the latent space,

$\mathbf{z}_1 = \mathbf{E}(\mathbf{x}_1)$, and then is used to condition the distribution over the latent representation of the desired view:

$$p_\theta(\mathbf{z}_2|\mathbf{z}_1, \mathbf{c}_{2,1}), \quad (5)$$

where $\mathbf{c}_{2,1}$ is the relative camera pose between the source and target views. The distribution is estimated using a diffusion model [33] with score function $\epsilon_\theta(\mathbf{z}_{2,t}, \mathbf{z}_1, t, \mathbf{c}_{2,1})$. The novel view, \mathbf{x}_2 , is then decoded from the sampled latent representation: $\mathbf{x}_2 = \mathbf{D}(\mathbf{z}_{2,T})$.

To obtain views along a trajectory with our model we generate them in sequence. Ideally, these would be sampled using the distribution conditioned on all previously generated views:

$$\mathbf{z}_{i+1} \sim p(\mathbf{z}_{i+1}|\mathbf{z}_0, \dots, \mathbf{z}_i, \mathbf{c}_{i+1,0}, \dots, \mathbf{c}_{i+1,i}). \quad (6)$$

We approximate this by assuming a Markov relationship between views in the sequence. That is, given an initial image, \mathbf{x}_0 , samples in the sequence of length L are obtained by encoding the initial image, $\mathbf{z}_0 = \mathbf{E}(\mathbf{x}_0)$, and recursively sampling from:

$$\mathbf{z}_{i+1} \sim p(\mathbf{z}_{i+1}|\mathbf{z}_i, \mathbf{c}_{i+1,i}), \quad (7)$$

with the final images decoded from the sampled latent representation: $\mathbf{x}_{L-1} = \mathbf{D}(\mathbf{z}_{L-1})$. We structure our model specifically for NVS, by equipping it with a specialized representation for relative camera geometry, and a two stream architecture.

Reasoning about novel views requires knowledge of geometric camera information. To provide this information we augment the input of the score function with a representation of the camera rays for the conditioning and generated views [40, 31]. Our camera model is defined by the intrinsic matrix, \mathbf{K} , and the extrinsics, $\mathbf{c} = [\mathbf{R}|\mathbf{t}]$, where \mathbf{R} and \mathbf{t} are the 3D rotation and translation components, respectively. Given the projection matrix of a camera, $\mathbf{P} = \mathbf{K}[\mathbf{R}|\mathbf{t}]$, the camera center is computed as $\boldsymbol{\tau} = -\mathbf{R}^{-1}\mathbf{t}$. The direction of the camera ray at pixel coordinates (u, v) is given by:

$$\bar{\mathbf{d}}_{u,v} = \mathbf{R}^{-1}\mathbf{K}^{-1} \begin{bmatrix} u & v & 1 \end{bmatrix}^\top, \quad (8)$$

which is then normalized to unit length to obtain $\mathbf{d}_{u,v}$. Finally, before used as conditioning for the diffusion model, the ray direction is concatenated with the camera center, $\mathbf{r}_{u,v} = [\mathbf{d}_{u,v}, \boldsymbol{\tau}]$, and frequency encoded [35]:

$$\mathcal{R} = [\sin(f_1\pi\mathbf{r}), \cos(f_1\pi\mathbf{r}), \dots, \sin(f_K\pi\mathbf{r}), \cos(f_K\pi\mathbf{r})], \quad (9)$$

where K is the number of frequencies, f_k are the frequencies which increase proportionally to 2^k , and the sinusoidal functions are applied element-wise.

The standard architecture for a score function is a U-Net architecture [29]. Here, we base our architecture on the

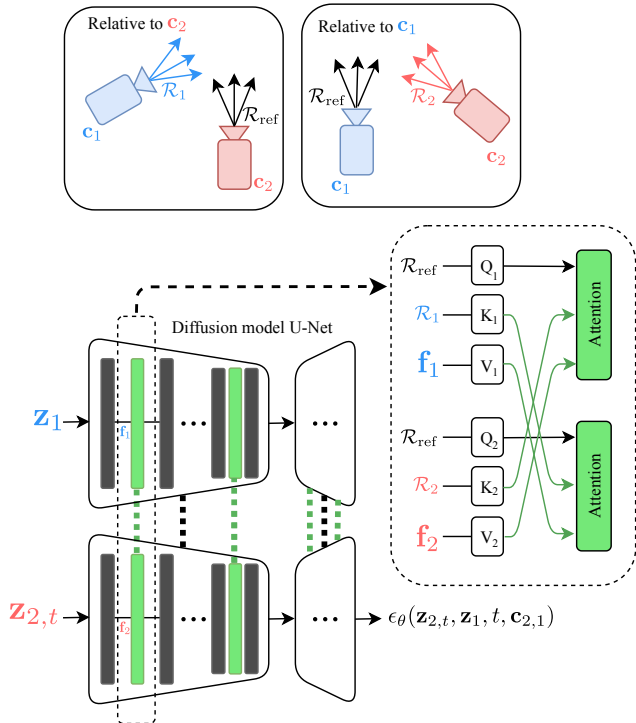


Figure 2: An overview of our model with two streams coupled with cross-attention. Our diffusion model is implemented as a U-Net, where latent representations for the given view, \mathbf{z}_1 (blue) and the generated view at diffusion step t , $\mathbf{z}_{2,t}$ (red), are processed by separate streams consisting of spatial layers with shared parameters (black). The latent of the given view, \mathbf{z}_1 is used to condition the score of $\mathbf{z}_{2,t}$, and the camera poses are \mathbf{c}_1 and \mathbf{c}_2 . Both streams are also conditioned on the noise variance, which is omitted for clarity. The two streams only communicate via cross-attention layers (green). The queries are augmented with rays in a canonical reference frame, \mathcal{R}_{ref} . The keys, \mathbf{K}_1 and \mathbf{K}_2 , are augmented with ray information, \mathcal{R}_1 and \mathcal{R}_2 , respectively, which are each localized in the reference frame of the opposite view, \mathbf{c}_2 and \mathbf{c}_1 , illustrated on the top. The inset on the middle-right provides a zoomed-in view of the cross-attention layer, where \mathbf{f}_1 and \mathbf{f}_2 are incoming features.

Noise Conditional Score Network++ (NCSN++) architecture [33], with a variance exploding forward process. We modify this backbone architecture to incorporate the ray representation and the conditioned view. Inspired by video diffusion models [12], we propose a two stream architecture using two U-Nets with shared weights to process the novel view, $\mathbf{x}_{2,t}$, and conditioning view, \mathbf{x}_1 . These networks communicate with one another exclusively via cross-attention layers, which are inserted after every spatial attention layer. We also augment the queries and keys of the attention with camera pose information. The output of the novel view stream is used as the output of the score function, $\epsilon_{\theta}(\mathbf{z}_{2,t}, \mathbf{z}_1, t, \mathbf{c}_{2,1})$. In short, the model contains

a stream for each view, and couples them using augmented cross-attention. Our architecture is illustrated in Fig. 2 and more details are given in Appendix A.

3.3. Thresholded Symmetric Epipolar Distance (TSED)

Existing evaluation metrics for NVS primarily focus on the view interpolation case and are based on notions of reconstruction (e.g., PSNR and LPIPS) or general image quality (e.g., FID); however, reconstruction metrics are inapplicable to view extrapolation, where there is no reasonable expectation of a single ground truth output. General image quality metrics are relevant for view extrapolation but existing measures like FID are insensitive to the accuracy of the geometry. That is, generated images can completely ignore the required camera pose and still achieve excellent FID. To address this issue recent work [38] proposed a metric that is sensitive to accurate camera geometry, but the evaluation involves fitting a NeRF [21] to multiple generated images, and measuring consistency as the FID of unseen interpolated views; however, this evaluation is complex, excessively expensive to compute, and difficult to interpret. Here, we propose the Thresholded Symmetric Epipolar Distance (TSED) as a new light weight metric for measuring geometric consistency of NVS models.

Our metric is motivated by two consistency criteria. First, the appearance of objects should remain stable between views, and should contain image features that can be identified and matched. Second, these matched features should respect epipolar constraints [8], given by the desired relative camera pose. With the camera poses used to condition the generation of the novel view, we compute the fundamental matrix, \mathbf{F} , which, given a feature point \mathbf{p} in one image, allows us to define the epipolar line $\mathbf{p}'^{\top} \mathbf{F} \mathbf{p} = 0$ on which its corresponding feature \mathbf{p}' should lie. We define the symmetric epipolar distance (SED) of corresponding points \mathbf{p} and \mathbf{p}' as:

$$\text{SED}(\mathbf{p}, \mathbf{p}', \mathbf{F}) = \frac{1}{2} [d(\mathbf{p}', \mathbf{F}\mathbf{p}) + d(\mathbf{p}, \mathbf{F}^{\top} \mathbf{p}')], \quad (10)$$

where $d(\mathbf{p}', \mathbf{F}\mathbf{p})$ is the minimum Euclidean distance between point \mathbf{p}' and the epipolar line induced by $\mathbf{F}\mathbf{p}$. We note this definition of SED is similar in spirit but slightly different than those found some standard references. Given a set of feature correspondences, $M = \{(\mathbf{p}_1, \mathbf{p}'_1), \dots, (\mathbf{p}_n, \mathbf{p}'_n)\}$, between two views (e.g., computed with SIFT [19]) we define the pair of images to be consistent if there are a sufficient number of matching features, i.e., $n \geq T_{\text{matches}}$, and the median SED over M is less than T_{error} . The median is chosen to mitigate the influence of incorrect correspondences. T_{matches} makes the metric robust against image pairs with few matches as this likely indicates a low-quality generation, assuming the scenes are

not largely textureless and the cameras do not undergo an extreme viewpoint change. The use of epipolar geometry here is key as it does not require knowledge of the scene geometry or scale. Given a NVS model, we evaluate it by generating sequences of images and computing which fraction of neighbouring views are consistent. We use $T_{\text{matches}} = 10$ and explore consistency as a function of different values of T_{error} in our experiments.

4. Experiments

In this section, we evaluate and compare to extant methods with a focus on *both* independent image quality and consistency across views. We conduct an ablation study on CLEVR [13], a synthetic dataset, to validate the various components of our model (Sec. 4.2). We further demonstrate the capabilities of our model using RealEstate10K [42], a large dataset of real indoor scenes, and compare our method with two strong baselines (Sec. 4.3): GeoGPT [28] and LookOut [25].

4.1. Experimental Setup

For our experiments, we implement our model using a latent diffusion model (LDM) [27] with a VQ-GAN [5] as the latent space autoencoder and a modified architecture as described in the previous section. During inference, we sample with ancestral sampling using a predictor-corrector sampler [33]. Training requires pairs of images along with camera intrinsics and relative extrinsics. For evaluation we use the CLEVR [13] and RealEstate10K [42] datasets.

CLEVR [13] is a synthetic dataset consisting of scenes of simple geometric primitives with various materials placed on top of a matte grey surface. We repurpose the Blender based pipeline to uniformly scatter the primitives in the center of the scene in an 8×8 Blender unit area, and render views from a slightly elevated position to prevent the camera from being placed inside an object. The initial camera position is chosen uniformly in the same area that the objects are placed, and oriented towards the center of the scene with a $[-20, 20]$ degree jitter around the yaw axis. For the second view, the camera is randomly translated $[-1, 1]$ units along the ground plane, and jittered $[-20, 20]$ degrees around the yaw axis. Images are rendered at a resolution of 128×128 . The left most panel in Fig. 4 provides an example image.

RealEstate10K [42] consists of publicly available real estate tour videos scraped from YouTube. The videos are partitioned into disjoint sequences, and the camera parameters provided with the dataset were recovered using ORB-SLAM2 [22]. The large amount of real, diverse, and structured environments available in RealEstate10K make it an ideal and commonly used dataset for NVS evaluation, including by the most relevant baselines [28, 25]. Following previous work [25], the videos are obtained at 360p, center

cropped, and downsampled to 256×256 . One challenging aspect of using this dataset is the limited diversity in camera motions. Many of the sequences consists of a simple forward motion that travels through and between rooms. This gives us an opportunity to evaluate the generalization of the model to novel camera motions not present in the dataset.

For our evaluations, we compare our method with two recent state-of-the-art generative scene extrapolation methods. GeoGPT [28] is an image-to-image NVS method, using a similar probabilistic formulation as our method. Four variants were proposed with options to leverage monocular depth maps provided by MiDaS [24], and perform explicit warping of the source image. For our evaluation, we use their model with implicit geometry and without access to depth maps as this is most similar to our proposed method, and can, similarly, be applied autoregressively to generate sequences. LookOut¹ [25] is an extension of GeoGPT with a focus on improving the generation of novel views over a long camera trajectory. The model takes up to two input frames of a sequence, and uses the camera pose information to explicitly bias the attention layers inside the model. The final LookOut model is fine-tuned with a form of simulated error accumulation [18] to make the model robust to errors present in its inputs during autoregressive generation. In our evaluation, we consider two variants of LookOut, one including this post-processing step (LookOut), and one without (LookOut-noerror). Note both GeoGPT and our model do not include a post-processing step and could potentially benefit from it.

In addition to our introduced consistency metric (Sec. 3.3), we evaluate the quality of the generated images using other standard image-centric metrics, specifically PSNR, LPIPS, and FID. PSNR and LPIPS are standard full reference image reconstruction metrics used to evaluate differences between generated and ground truth views. However, as the camera view changes significantly the space of plausible views increases dramatically and reconstruction metrics like PSNR and LPIPS become less relevant due to a lack of single ground truth reference. While these metrics are not suitable for evaluating view extrapolation tasks [34, 26], they can still provide some sense of consistency for short-term generation, where uncertainty in the novel views is low. FID [9] is a standard reference-free metric for generative methods which measures sample quality of a set of i.i.d. samples, compared to a set of real samples. While FID does not provide a measure of consistency between images, it gives a sense of the overall realism of the generated images.

¹An official public implementation is available without the pretrained weights on RealEstate10k. After email correspondence with the authors, we were unable to obtain the pretrained model. Reported results are based on a retrained model using the authors’ publicly available code.

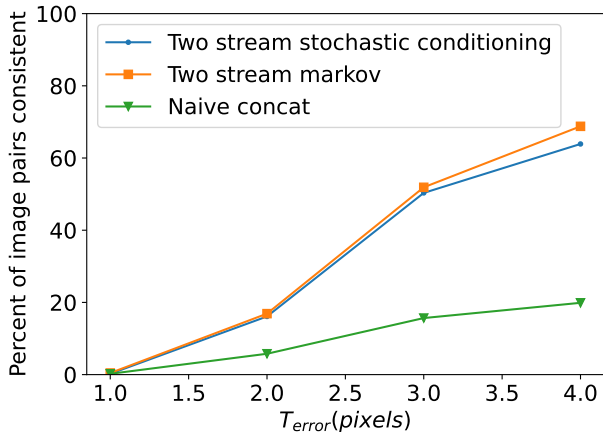


Figure 3: Percent consistent image pairs computed with TSED on different variants of our model, and sampling, on CLEVR.

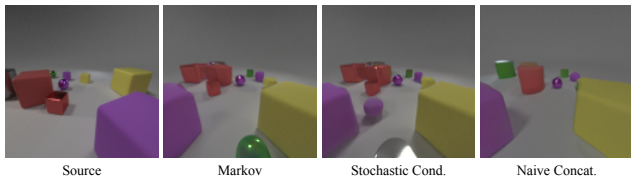


Figure 4: Samples of the sixth generated frame from the initial image on the left. Note the small red cube visible in the initial image disappears for the naive model.

Method	Single view		Last view
	LPIPS ↓	PSNR ↑	FID ↓
Naive concat	0.121	23.24	79.57
Two Stream SC	-	-	78.11
Two Stream	0.112	24.20	76.85

Table 1: Reconstruction metrics and FID for single view prediction, and sequential prediction on CLEVR. *Two Stream* is our two stream model, *Two Stream SC* is our two stream model sampled with stochastic conditioning, and *Naive concat* is the naive variant where inputs are concatenated along the channel dimension. We evaluate the FID on the last generated image of a trajectory. Stochastic conditioning is only applicable with more than two generated views, no results are provided for this method on single view evaluations.

4.2. Ablations

Here, we explore variations on model architecture and sampling, and compare performance. First, we compare our two stream architecture with a naive conditional diffusion model architecture, where both source and target views are concatenated to create a six channel image, and the

model estimates the score for the target view. The results are shown in Table 1 which show clearly that our proposed architecture is effective.

We also explore an alternative strategy to sampling trajectories of novel views. Previous work [38] proposed a heuristic for extending a single source view novel view diffusion model to use an arbitrary number of source views called *stochastic conditioning*. Given m possible source views, each iteration of the diffusion sampling process is modified to be randomly conditioned on one of the m views. We consider this heuristic for generating sets of views, conditioning on up to two of the previous frames. For these ablations we sample ten images from a trajectory orbiting the center of the scene, using 100 different starting images.

We evaluate consistency using TSED, quantitative results are provided in Fig. 3, and qualitative results are shown in Fig. 4. We find that the naive model can generate images where clearly visible objects may disappear, leading to less consistency qualitatively and quantitatively. Sampling with stochastic conditioning is qualitatively similar to Markov sampling. Quantitatively, stochastic conditioning is less consistent when T_{error} is high, which is the result of fewer matches being made. In general, recovering correspondences on CLEVR is challenging due to few distinct features. Despite the challenges presented by this dataset, our metric is still able to provide a measure of consistency. Overall, these results show that, in contrast to [38], stochastic conditioning has no positive benefit to our approach and may actually hurt performance. We also attempt to perform stochastic conditioning on RealEstate10K, but the images are qualitative poor, results are available in Appendix B.

4.3. Generation with In-Distribution Trajectories

For our initial set of experiments on RealEstate10K, we consider the generation of novel views along in-distribution trajectories. To generate representative, in-distribution trajectories, given a start image, we randomly sample camera trajectories from the test set, as done in previous work [25].

Image quality. We evaluate the reconstruction performance of novel views using PSNR, and LPIPS, across short-term and long-term generations. Following previous work [25], we only consider test sequences where at least 200 frames are available. This choice ensures that there are ground truth images to evaluate against. Starting with the first frame from the ground truth test sequences as our initial images, we generate 20 images of a sequence using 20 camera poses of the ground truth trajectory. The camera poses are spaced ten frames apart with respect to the sequence’s native frame rate, yielding a final camera pose that is 200 frames from the initial view. Short-term evaluations are performed over the fifth generated image, and long-term evaluations are performed on the final generated image. Quantitative results are available in Table 2. Compared to the baselines, our

Method	Short-term		Long-term	
	LPIPS ↓	PSNR ↑	LPIPS ↓	PSNR ↑
GeoGPT [28]	0.444	13.35	0.674	9.54
LookOut-noerror [25]	0.390	14.19	0.688	9.65
LookOut [25]	0.378	14.43	0.658	10.51
Ours	0.333	15.51	0.588	11.54

Table 2: Short and long-term reconstruction error on in-distribution trajectories for RealEstate10K. LookOut-noerror refers to the LookOut method without the final error accumulation training step.

method has the lowest reconstruction error in all cases. We also evaluate LookOut [25] without their additional post-processing step (LookOut-noerror), and find that it yields slightly worse reconstruction results.

Similar to our full reference metric evaluation above, we evaluate short-term and long-term quality with the no-reference metric FID. To measure the quality of generation over time, we evaluate the FID between generated views at a specific time, and a fixed set of randomly selected views from the test set. Quantitative results are shown in Table 3. All methods suffer from some level of error accumulation, and yield worse performance as the sequence length increases. We find that LookOut produces images with significantly higher FID without the final error accumulation step. For in-distribution trajectories, our method generates images with comparable quality as GeoGPT, and outperforms LookOut, in terms of FID. Notably, GeoGPT has the tendency to generate viewpoint inconsistent images, where the semantics remain the same but the content changes. This point is examined next using our viewpoint consistency metric.

Consistency over long-term generations. Using our proposed metric, TSED (Sec. 3.3), we evaluate the percent of consistent pairs of neighboring views out of 20 total pairs. Quantitative results are shown in Fig. 5, where we evaluate the consistency over a range of values for T_{error} , with $T_{matches} = 10$. The average number of matches per pair is 33, 87, and 94, for GeoGPT, LookOut, and our method, respectively. The lower consistency of GeoGPT is partly due to fewer matches per image pair. Samples from LookOut have a comparable number of matches to our method, suggesting that the inconsistency is due to larger violations of the epipolar constraints. Compared to the baselines, our method can generate better views with consistent appearances, and motion that respects epipolar constraints. LookOut performs similarly on our consistency metric with and without error accumulation training.

4.4. Generation with Novel Trajectories

Previous work limited evaluation to ground truth trajectories in the RealEstate10K dataset. Consequently, given the biased nature of the trajectories, this may lead to overfitting. Here, we explore the generalization capability of

Method	Short-term FID ↓	Long-term FID ↓
GeoGPT [28]	26.72	41.87
LookOut-noerror [25]	30.38	72.01
LookOut [25]	28.86	58.12
Ours	26.76	41.95

Table 3: FID scores between generated images at short and long term generations, and a fixed set of randomly selected images from the RealEstate10K test set. Generated images are along in-distribution trajectories.

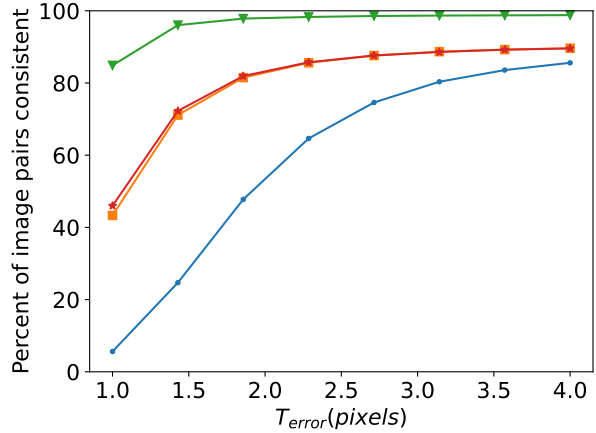


Figure 5: Consistency as the percent of consistent image pairs for in-distribution trajectories. We set $T_{matches} = 10$.

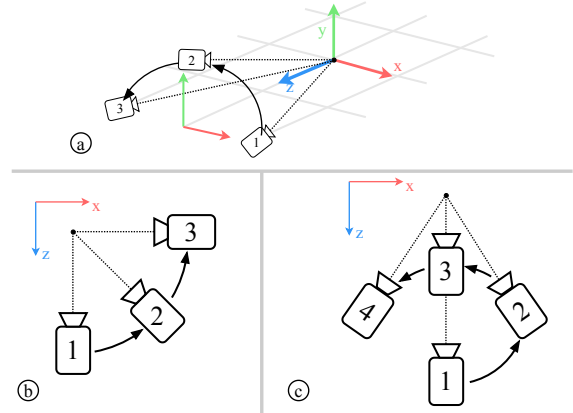


Figure 6: A visualization of our custom trajectories: hop (a), orbit (b), and spin (c). All cameras point towards a pivot in the scene, and the dotted lines represent the optical axes of the cameras. We use a coordinate space where x is right, y is up, and z is backward.

both our method and the baselines by evaluating on out-of-distribution trajectories.

As mentioned in Section 4.1, the camera motions available in RealEstate10K are limited. Samples from out-of-distribution trajectories can be obtained by sampling autoregressively, while ensuring that the relative poses of neigh-

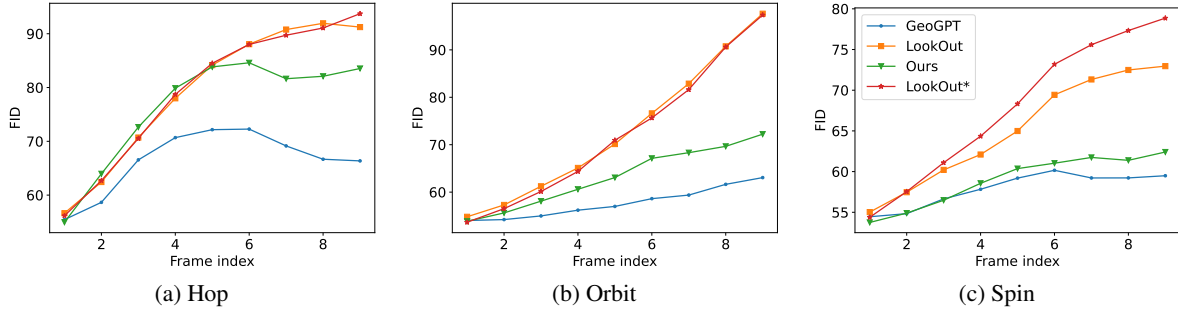


Figure 7: FID scores between generated views at a specific time, and a fixed set of randomly selected views from the RealEstate10K test set. Sequences are sampled using three novel trajectories designed to differ from the dominant modes in the dataset: Hop, Orbit, and Spin. *LookOut** is a version of LookOut without error accumulation post-processing.

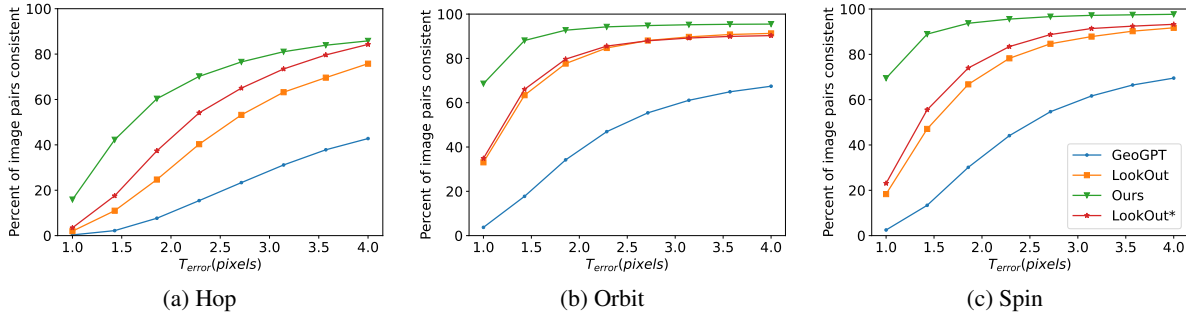


Figure 8: Plots for TSED over a range of T_{error} values, with $T_{matches} = 10$, for our three custom trajectories: Hop, Orbit, and Spin. *LookOut** is a version of LookOut without error accumulation post-processing.



Figure 9: Samples from the *orbit* trajectory. Each row presents a generated image sequence from our method and the baselines, GeoGPT [28] and LookOut [25]. The columns, are sampled views along the trajectory with the left most image being given. Notice both baselines give the impression of an orbiting camera motion, but parts of the visible scene in both views change between frames, *i.e.*, the cabinet under the sink. Images generated from LookOut tend to lose details in subsequent frames. Our method tends to maintain photometric consistency across the sequence.

boring views are in-distribution. We sample novel views over three manually defined trajectories distinct from those found in RealEstate10K: (i) a 90 degree orbit around the azimuth (orbit), (ii) a vertical orbit along a semicircular path (hop), and (iii) a translation along a circular path parallel to the ground plane (spin). These trajectories are illustrated in Fig. 6.

As ground truth images are not available, we evaluate performance using the reference-free metrics, FID and TSED. Quantitative results are summarized in Figs. 7 and 8. In terms of FID, our model’s generation quality degrades faster than GeoGPT, but slower than LookOut. Qualitative results such as those shown in Fig. 9, suggest that when the baseline methods fail, they favour generating good quality images, even though they may not be photometrically consistent with the other views. The consistency of our generated sequences, evaluated using TSED, is higher than the baselines on all trajectories. Between the three custom trajectories, *hop* is the most novel as it contains a vertical motion that is rare in RealEstate10K, while *spin* is the closest to the training trajectories which contain many forward and backward motions. Interestingly, LookOut without error accumulation performs better in the *hop* trajectory on TSED. This suggests that the error accumulation post-processing may trade off generalization for higher image quality. Overall, our method provides the best trade off of photometric quality and consistency.

5. Conclusion and Discussion

We addressed the most challenging setting for NVS, i.e., generative view extrapolation from a single image. Our method exploits recent advancements in diffusion-based generative models to sample multiple consistent novel views. Empirically, we presented a finer-grained evaluation of the task compared to previous studies. In particular, reported results of previous work focus on generated image quality of each image, but ignore geometric consistency. Here, we introduced a new metric based on epipolar geometry, which directly evaluates geometric consistency of generated views independent of image quality. Based on our new metric and standard ones, we showed that our method generates images that are more consistent than current methods, while maintaining high image quality. Further, on camera trajectories that are atypical of the training data, we showed that our method generates images that are more consistent than the baselines.

Acknowledgement. This work was funded in part by the Canada First Research Excellence Fund (CFREF) for the Vision: Science to Applications (VISTA) program, the NSERC Discovery Grant program, the NSERC Canada Graduate Scholarships – Doctoral program, and the Vector Institute for AI.

References

- [1] Shai Avidan and Amnon Shashua. Novel view synthesis in tensor space. In *Proceedings of the IEEE Conference on Computer Vision and Pattern Recognition (CVPR)*, pages 1034–1040, 1997. 1, 2
- [2] Miguel Ángel Bautista, Pengsheng Guo, Samira Abnar, Walter Talbott, Alexander T Toshev, Zhuoyuan Chen, Laurent Dinh, Shuangfei Zhai, Hanlin Goh, Daniel Ulbricht, Afshin Dehghan, and Joshua M. Susskind. GAUDI: A neural architect for immersive 3d scene generation. In *Neural Information Processing Systems (NeurIPS)*, 2022. 2
- [3] Andrew Brock, Jeff Donahue, and Karen Simonyan. Large scale gan training for high fidelity natural image synthesis. *arXiv preprint arXiv:1809.11096*, 2018. 12
- [4] Shenchang Eric Chen and Lance Williams. View interpolation for image synthesis. In *Proceedings of SIGGRAPH*, pages 279–288, 1993. 1, 2
- [5] Patrick Esser, Robin Rombach, and Bjorn Ommer. Taming transformers for high-resolution image synthesis. In *Proceedings of the IEEE Conference on Computer Vision and Pattern Recognition (CVPR)*, pages 12873–12883, 2021. 2, 5
- [6] Ian Goodfellow, Jean Pouget-Abadie, Mehdi Mirza, Bing Xu, David Warde-Farley, Sherjil Ozair, Aaron Courville, and Yoshua Bengio. Generative adversarial nets. In *Neural Information Processing Systems (NeurIPS)*, volume 27. Curran Associates, Inc., 2014. 2
- [7] Florentin Guth, Simon Coste, Valentin De Bortoli, and Stephane Mallat. Wavelet score-based generative modeling. *Neural Information Processing Systems (NeurIPS)*, 2022. 3
- [8] Richard Hartley and Andrew Zisserman. *Multiple View Geometry in Computer Vision*. Cambridge university press, 2003. 2, 4, 14
- [9] Martin Heusel, Hubert Ramsauer, Thomas Unterthiner, Bernhard Nessler, and Sepp Hochreiter. GANs trained by a two time-scale update rule converge to a local nash equilibrium. In *Neural Information Processing Systems (NeurIPS)*, volume 30. Curran Associates, Inc., 2017. 2, 5
- [10] Jonathan Ho, Ajay Jain, and Pieter Abbeel. Denoising diffusion probabilistic models. *Neural Information Processing Systems (NeurIPS)*, 33:6840–6851, 2020. 2, 3
- [11] Jonathan Ho, Chitwan Saharia, William Chan, David J Fleet, Mohammad Norouzi, and Tim Salimans. Cascaded diffusion models for high fidelity image generation. *Journal of Machine Learning Research*, 2022. 3
- [12] Jonathan Ho, Tim Salimans, Alexey Gritsenko, William Chan, Mohammad Norouzi, and David J Fleet. Video diffusion models. *Proceedings of the International Conference on Learning Representations (ICLR)*, 2022. 2, 4
- [13] Justin Johnson, Bharath Hariharan, Laurens Van Der Maaten, Li Fei-Fei, C Lawrence Zitnick, and Ross Girshick. Clevr: A diagnostic dataset for compositional language and elementary visual reasoning. In *Proceedings of the IEEE Conference on Computer Vision and Pattern Recognition (CVPR)*, pages 2901–2910, 2017. 5, 12

- [14] Diederik P. Kingma and Max Welling. Auto-encoding variational bayes. In *Proceedings of the International Conference on Learning Representations (ICLR)*, 2014. 2
- [15] Jing Yu Koh, Harsh Agrawal, Dhruv Batra, Richard Tucker, Austin Waters, Honglak Lee, Yinfei Yang, Jason Baldridge, and Peter Anderson. Simple and effective synthesis of indoor 3D scenes. *Proceedings of the National Conference on Artificial Intelligence (AAAI)*, 2023. 2
- [16] Stephane Laveau and Olivier D Faugeras. 3-D scene representation as a collection of images. In *Proceedings of the International Conference on Pattern Recognition (ICPR)*, volume 1, pages 689–691, 1994. 1, 2
- [17] Alex X. Lee, Richard Zhang, Frederik Ebert, Pieter Abbeel, Chelsea Finn, and Sergey Levine. Stochastic adversarial video prediction. *Proceedings of the International Conference on Learning Representations (ICLR)*, 2019. 2
- [18] Andrew Liu, Richard Tucker, Varun Jampani, Ameesh Makadia, Noah Snavely, and Angjoo Kanazawa. Infinite nature: Perpetual view generation of natural scenes from a single image. In *Proceedings of the International Conference on Computer Vision (ICCV)*, pages 14458–14467, 2021. 2, 5
- [19] David G Lowe. Object recognition from local scale-invariant features. In *Proceedings of the International Conference on Computer Vision (ICCV)*, volume 2, pages 1150–1157, 1999. 4, 14
- [20] Chenlin Meng, Yutong He, Yang Song, Jiaming Song, Jiajun Wu, Jun-Yan Zhu, and Stefano Ermon. SDEdit: Guided image synthesis and editing with stochastic differential equations. In *Proceedings of the International Conference on Learning Representations (ICLR)*, 2022. 2
- [21] Ben Mildenhall, Pratul P. Srinivasan, Matthew Tancik, Jonathan T. Barron, Ravi Ramamoorthi, and Ren Ng. NeRF: Representing scenes as neural radiance fields for view synthesis. In *Proceedings of the European Conference on Computer Vision (ECCV)*, 2020. 2, 4
- [22] Raul Mur-Artal, Jose Maria Martinez Montiel, and Juan D Tardos. ORB-SLAM: A versatile and accurate monocular slam system. *IEEE Transactions on Robotics (T-RO)*, 31(5):1147–1163, 2015. 5
- [23] Weili Nie, Arash Vahdat, and Anima Anandkumar. Controllable and compositional generation with latent-space energy-based models. In *Neural Information Processing Systems (NeurIPS)*, volume 34, pages 13497–13510, 2021. 2, 3
- [24] René Ranftl, Katrin Lasinger, David Hafner, Konrad Schindler, and Vladlen Koltun. Towards robust monocular depth estimation: Mixing datasets for zero-shot cross-dataset transfer. *IEEE Transactions on Pattern Analysis and Machine Intelligence (PAMI)*, 44(3), 2022. 5
- [25] Xuanchi Ren and Xiaolong Wang. Look outside the room: Synthesizing a consistent long-term 3D scene video from a single image. In *Proceedings of the IEEE Conference on Computer Vision and Pattern Recognition (CVPR)*, pages 3563–3573, 2022. 2, 5, 6, 7, 8, 14
- [26] Chris Rockwell, David F Fouhey, and Justin Johnson. Pixel-synth: Generating a 3D-consistent experience from a single image. In *Proceedings of the International Conference on Computer Vision (ICCV)*, pages 14104–14113, 2021. 5
- [27] Robin Rombach, Andreas Blattmann, Dominik Lorenz, Patrick Esser, and Björn Ommer. High-resolution image synthesis with latent diffusion models. In *Proceedings of the IEEE Conference on Computer Vision and Pattern Recognition (CVPR)*, pages 10684–10695, 2022. 2, 3, 5
- [28] Robin Rombach, Patrick Esser, and Björn Ommer. Geometry-free view synthesis: Transformers and no 3D priors. In *Proceedings of the International Conference on Computer Vision (ICCV)*, pages 14356–14366, 2021. 2, 5, 7, 8, 14
- [29] Olaf Ronneberger, Philipp Fischer, and Thomas Brox. U-net: Convolutional networks for biomedical image segmentation. In *Proceedings of the International Conference on Medical Image Computing and Computer Assisted Intervention (MICCAI)*, pages 234–241, 2015. 3
- [30] Chitwan Saharia, William Chan, Saurabh Saxena, Lala Li, Jay Whang, Emily Denton, Seyed Kamyar Seyed Ghasemipour, Raphael Gontijo-Lopes, Burcu Karagol Ayan, Tim Salimans, Jonathan Ho, David J. Fleet, and Mohammad Norouzi. Photorealistic text-to-image diffusion models with deep language understanding. In *Neural Information Processing Systems (NeurIPS)*, 2022. 2
- [31] Mehdi S. M. Sajjadi, Henning Meyer, Etienne Pot, Urs Bergmann, Klaus Greff, Noha Radwan, Suhani Vora, Mario Lucic, Daniel Duckworth, Alexey Dosovitskiy, Jakob Uszkoreit, Thomas Funkhouser, and Andrea Tagliasacchi. Scene representation transformer: Geometry-free novel view synthesis through set-latent scene representations. In *Proceedings of the IEEE Conference on Computer Vision and Pattern Recognition (CVPR)*, pages 6229–6238, 2022. 2, 3
- [32] Tim Salimans, Andrej Karpathy, Xi Chen, and Diederik P. Kingma. PixelCNN++: Improving the pixelCNN with discretized logistic mixture likelihood and other modifications. In *Proceedings of the International Conference on Learning Representations (ICLR)*, 2017. 2
- [33] Yang Song, Jascha Sohl-Dickstein, Diederik P Kingma, Abhishek Kumar, Stefano Ermon, and Ben Poole. Score-based generative modeling through stochastic differential equations. In *Proceedings of the International Conference on Learning Representations (ICLR)*, 2021. 2, 3, 4, 5, 12
- [34] Piotr Teterwak, Aaron Sarna, Dilip Krishnan, Aaron Maschinot, David Belanger, Ce Liu, and William T Freeman. Boundless: Generative adversarial networks for image extension. In *Proceedings of the International Conference on Computer Vision (ICCV)*, pages 10521–10530, 2019. 5
- [35] Ashish Vaswani, Noam Shazeer, Niki Parmar, Jakob Uszkoreit, Llion Jones, Aidan N Gomez, Łukasz Kaiser, and Illia Polosukhin. Attention is all you need. *Neural Information Processing Systems (NeurIPS)*, 30, 2017. 3
- [36] Dor Verbin, Peter Hedman, Ben Mildenhall, Todd Zickler, Jonathan T Barron, and Pratul P Srinivasan. Ref-nerf: Structured view-dependent appearance for neural radiance fields. In *Proceedings of the IEEE Conference on Computer Vision and Pattern Recognition (CVPR)*, pages 5481–5490, 2022. 2
- [37] Pascal Vincent. A connection between score matching and denoising autoencoders. *Neural computation*, 23(7):1661–1674, 2011. 3

- [38] Daniel Watson, William Chan, Ricardo Martin-Brualla, Jonathan Ho, Andrea Tagliasacchi, and Mohammad Norouzi. Novel view synthesis with diffusion models. *Proceedings of the International Conference on Learning Representations (ICLR)*, 2023. [2](#), [4](#), [6](#), [12](#), [13](#)
- [39] Ling Yang, Zhilong Zhang, Yang Song, Shenda Hong, Runsheng Xu, Yue Zhao, Yingxia Shao, Wentao Zhang, Ming-Hsuan Yang, and Bin Cui. Diffusion models: A comprehensive survey of methods and applications. *CoRR*, abs/2209.00796, 2022. [3](#)
- [40] Wang Yifan, Carl Doersch, Relja Arandjelović, João Carreira, and Andrew Zisserman. Input-level inductive biases for 3D reconstruction. In *Proceedings of the IEEE Conference on Computer Vision and Pattern Recognition (CVPR)*, pages 6176–6186, 2022. [3](#)
- [41] Alex Yu, Vickie Ye, Matthew Tancik, and Angjoo Kanazawa. pixelNeRF: Neural radiance fields from one or few images. In *Proceedings of the IEEE Conference on Computer Vision and Pattern Recognition (CVPR)*, pages 4578–4587, 2021. [2](#)
- [42] Tinghui Zhou, Richard Tucker, John Flynn, Graham Fyffe, and Noah Snavely. Stereo magnification: Learning view synthesis using multiplane images. In *ACM Transactions on Graphics (TOG)*, 2018. [5](#), [12](#)

Layer	Output size	Additional inputs	Additional outputs
Input image	$4 \times 32 \times 32$		Skip 0, In Pyramid
ResBlock	$256 \times 32 \times 32$	Time emb.	
Spatial Attn.	$256 \times 32 \times 32$		
Cross Attn.	$256 \times 32 \times 32$	Cross, Rays	Skip 1, Cross
ResBlock	$256 \times 32 \times 32$	Time emb.	
Spatial Attn.	$256 \times 32 \times 32$		
Cross Attn.	$256 \times 32 \times 32$	Cross, Rays	Skip 2, Cross
ResBlockDown	$256 \times 16 \times 16$	Time emb.	
Combiner	$256 \times 16 \times 16$	In Pyramid 1	Skip 3
ResBlock	$256 \times 16 \times 16$	Time emb.	
Spatial Attn.	$256 \times 16 \times 16$		
Cross Attn.	$256 \times 16 \times 16$	Cross, Rays	Skip 4, Cross
ResBlock	$256 \times 16 \times 16$	Time emb.	
Spatial Attn.	$256 \times 16 \times 16$		
Cross Attn.	$256 \times 16 \times 16$	Cross, Rays	Skip 5, Cross
ResBlockDown	$256 \times 8 \times 8$	Time emb.	
Combiner	$256 \times 8 \times 8$	In Pyramid 2	Skip 6
ResBlock	$256 \times 8 \times 8$	Time emb.	
Spatial Attn.	$256 \times 8 \times 8$		
Cross Attn.	$256 \times 8 \times 8$	Cross, Rays	Skip 7, Cross
ResBlock	$256 \times 8 \times 8$	Time emb.	
Spatial Attn.	$256 \times 8 \times 8$		
Cross Attn.	$256 \times 8 \times 8$	Cross, Rays	Skip 8, Cross
ResBlockDown	$256 \times 4 \times 4$	Time emb.	
Combiner	$256 \times 4 \times 4$	In Pyramid 3	Skip 9
ResBlock	$256 \times 4 \times 4$	Time emb.	
Spatial Attn.	$256 \times 4 \times 4$		
Cross Attn.	$256 \times 4 \times 4$	Cross, Rays	Skip 10, Cross
ResBlock	$256 \times 4 \times 4$	Time emb.	
Spatial Attn.	$256 \times 4 \times 4$		
Cross Attn.	$256 \times 4 \times 4$	Cross, Rays	Skip 11, Cross
ResBlock	$256 \times 4 \times 4$	Time emb.	
Spatial Attn.	$256 \times 4 \times 4$		
ResBlock	$256 \times 4 \times 4$	Time emb.	

Table A.1: NSCN++ U-Net backbone encoder. The ResBlocks are BigGAN [3] style residual blocks, ResBlocksDown layers are the same, but configured with a downsampling option. Time embeddings (emb.) is the time information provided for the diffusion model. Skip inputs are skip connections that go to the decoder. Rays are the camera ray conditioning, and Cross is a cross-attention connection to the other stream.

A. Architecture Details

In this section, we provide additional details of our model described in Section 3.2 of the main paper. Our model is based on *Noise Conditional Score Network++* (NCSN++) [33]. An overview of the main backbone is provided in Tables A.1 and A.2. Two streams of the backbone are used to process the conditioning and generated image. We modify the original architecture by adding cross-attention layers throughout the backbone, which attend to features in the opposite stream. The residual blocks are based on the residual blocks used in BigGAN [3]. Upsampling and downsampling is also performed in the network using BigGAN residual blocks [3]. Inputs to the backbone encoder are provided at various layers using a multi-scale pyramid. Outputs of the network are accumulated from multiple layers of the decoder using a multi-scale residual pyramid. Specific implementation details can be found in the code release: <https://yorkucvil.github.io/Photoconsistent-NVS/>.

B. Stochastic Conditioning on RealEstate10K

Previous work [38] proposed a heuristic for extending a novel view diffusion model to use an arbitrary number of source views, called *stochastic conditioning*. Given m possible source views, each iteration of the diffusion sampling process is modified to be randomly conditioned on one of the m views. Results using stochastic conditioning on CLEVR [13] are provided in the main paper in Section 4.2. Previous work [38] used stochastic conditioning to condition on all previous frames. We also apply this heuristic for generating sets of views on RealEstate10K [42], but we condition on up to two of the previous frames. Qualitative results shown in Figure B.1 exhibit a significant reduction in quality, and contain noticeable

Layer	Output size	Additional inputs	Additional outputs
Encoder input	$256 \times 4 \times 4$		
ResBlock	$256 \times 4 \times 4$	Time emb., Skip 11	
ResBlock	$256 \times 4 \times 4$	Time emb., Skip 10	
ResBlock	$256 \times 4 \times 4$	Time emb., Skip 9	
Spatial Attn.	$256 \times 4 \times 4$		
Cross Attn.	$256 \times 4 \times 4$	Cross, Rays	Cross
Conv3 \times 3	$256 \times 4 \times 4$	Out Pyramid 1	
ResBlockUp	$256 \times 8 \times 8$	Time emb.	
ResBlock	$256 \times 8 \times 8$	Time emb., Skip 8	
ResBlock	$256 \times 8 \times 8$	Time emb., Skip 7	
ResBlock	$256 \times 8 \times 8$	Time emb., Skip 6	
Spatial Attn.	$256 \times 8 \times 8$		
Cross Attn.	$256 \times 8 \times 8$	Cross, Rays	Cross
Conv3 \times 3	$256 \times 8 \times 8$	Out Pyramid 2	
ResBlockUp	$256 \times 16 \times 16$	Time emb.	
ResBlock	$256 \times 16 \times 16$	Time emb., Skip 5	
ResBlock	$256 \times 16 \times 16$	Time emb., Skip 4	
ResBlock	$256 \times 16 \times 16$	Time emb., Skip 3	
Spatial Attn.	$256 \times 16 \times 16$		
Cross Attn.	$256 \times 16 \times 16$	Cross, Rays	Cross
Conv3 \times 3	$256 \times 16 \times 16$	Out Pyramid 3	
ResBlockUp	$256 \times 32 \times 32$	Time emb.	
ResBlock	$256 \times 32 \times 32$	Time emb., Skip 2	
ResBlock	$256 \times 32 \times 32$	Time emb., Skip 1	
ResBlock	$256 \times 32 \times 32$	Time emb., Skip 0	
Spatial Attn.	$256 \times 32 \times 32$		
Cross Attn.	$256 \times 32 \times 32$	Cross, Rays	Cross
Conv3 \times 3	$256 \times 32 \times 32$	Out Pyramid 4	

Table A.2: NSCN++ U-Net backbone decoder. The ResBlocks are BigGAN [3] style residual blocks, ResBlocksUp layers are the same, but configured with an upsampling option. Time embeddings (emb.) is the time information provided for the diffusion model. Skip inputs are skip connections coming from the encoder. Rays are the camera ray conditioning, and Cross is the cross-attention connection to the other stream.

artifacts. As a consequence, we do not include results based on stochastic conditioning with our method.



Figure B.1: Comparison of generation using a Markov dependency versus stochastic conditioning [38] with the previous two frames as input. Both methods were generated using the same trajectory and source image. In general, there is a significant reduction of quality when stochastic conditioning is applied.

C. Additional Qualitative Results

Additional qualitative results are provided with an interactive viewer on our project page at <https://yorkucvil.github.io/Photoconsistent-NVS/>, under the **Qualitative Results: Out-of-Distribution Trajectories** and **Qualitative Results: In-Distribution Trajectories** sections. The viewer allows the images along a trajectory to be explored for multiple scenes, and sampling instances. Due to the stochastic nature of our model and the baselines, different plausible extrapolations of the scene are shown in the different instances of sampling.

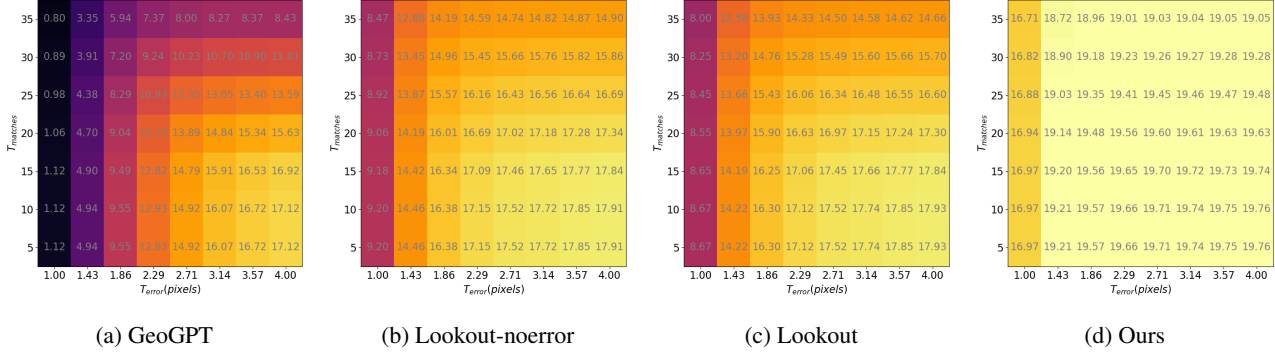


Figure D.1: TSED computed using images generated over in-distribution trajectories. We sweep over a range of values for T_{matches} and T_{error} . The values are provided as the average number of consistent pairs per sequence out of twenty.

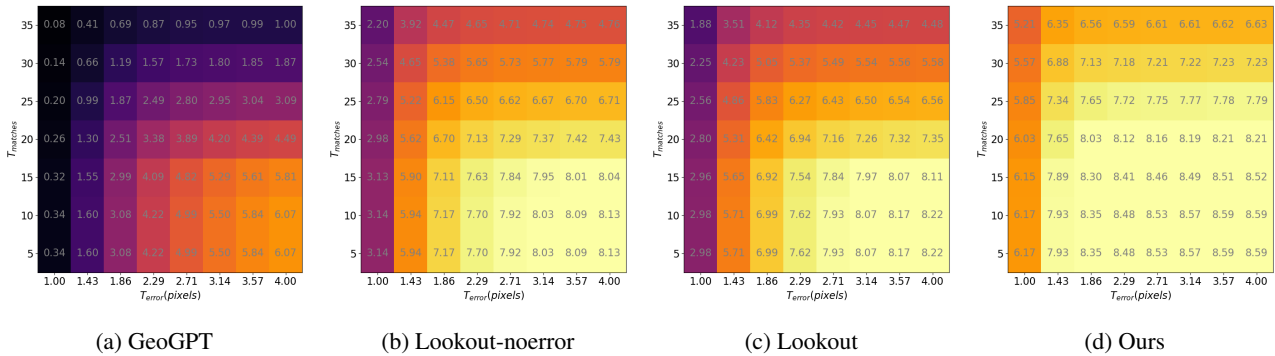


Figure D.2: TSED computed using images generated over *orbit* trajectory. We sweep over a range of values for T_{matches} and T_{error} . The values are provided as the average number of consistent pairs per sequence out of nine.

D. Additional Results with TSED

We provide additional quantitative results using TSED in Figures D.1, D.2, D.3, and D.4 for images generated using in-distribution trajectories, and the orbit, spin, hop out-of-distribution trajectories, respectively. Sequences using in-distribution trajectories consist of 21 frames, while sequences on our custom trajectories consist of 10 frames. We sweep across a range of values for both T_{error} and T_{matches} . Pairs of images with less than T_{matches} SIFT [19] matches, or a median SED [8] lower than T_{error} , are considered not consistent. In all trajectory types, GeoGPT [28] is the most affected by T_{matches} due to a lack of photometric consistency, which leads to a low number of SIFT correspondences. The TSED for both variants of Lookout [25] do not vary as severely as GeoGPT with respect to T_{matches} . Image pairs generated with our method tend to yield more SIFT matches, and are mainly affected by T_{error} . The quantitative TSED results in the main paper were evaluated at $T_{\text{matches}} = 10$, but these extended results show that our method yields higher TSED scores, remains consistent over a range of T_{matches} values, in all cases.

To provide a better intuition on how symmetric epipolar distance (SED) [8] provides a measure of consistency, we provide an interactive demo on our project page at <https://yorkucvil.github.io/Photoconsistent-NVS/>, under the **Visualization of SED** section. The demo visualizes how SED varies in response to the positions of two correspondences in a pair of views with known relative camera geometry. Each point creates an epipolar line on the opposite image, and the minimal distance line between a point and a line on the same image is shown.

E. Limitations of Autoregressive Sampling

Our method and the baselines are limited by the use of sequential generation with a fixed budget for conditioning images. Regions that become occluded and subsequently disoccluded in a sequence are very likely to change appearance. For example, conditioning on one image prevents information about previously disoccluded regions from informing the

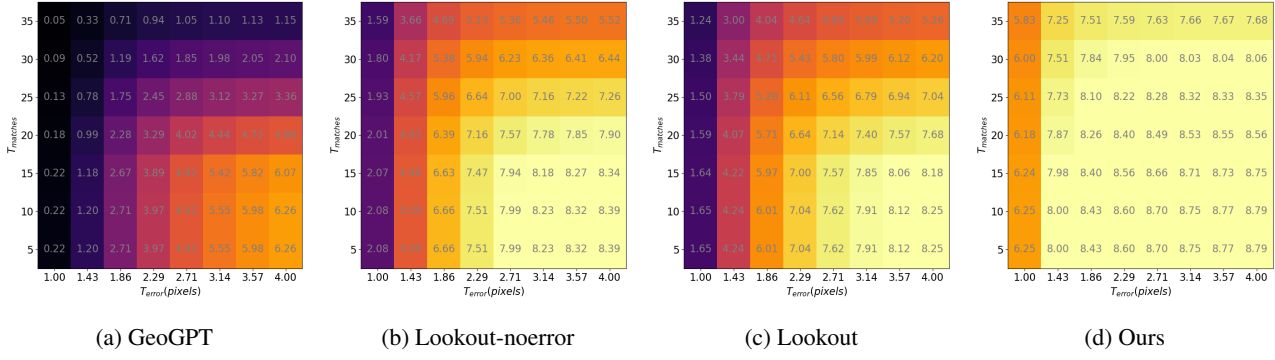


Figure D.3: TSED computed using images generated over *spin* trajectory. We sweep over a range of values for T_{matches} and T_{error} . The values are provided as the average number of consistent pairs per sequence out of nine.

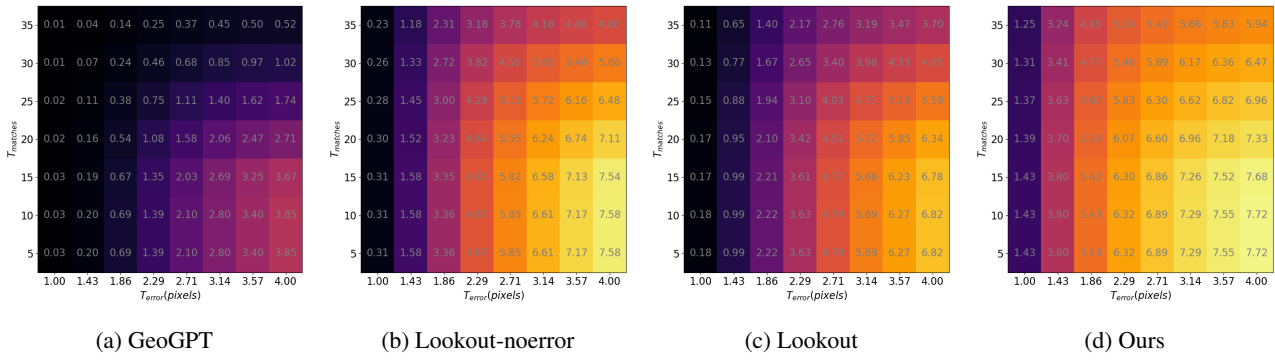


Figure D.4: TSED computed using images generated over our *hop* trajectory. We sweep over a range of values for T_{matches} and T_{error} . The values are provided as the average number of consistent pairs per sequence out of nine.

generation of those same regions beyond one frame. Qualitative examples of this phenomenon can be seen in the <https://yorkucvil.github.io/Photoconsistent-NVS/> under the **Qualitative Results: Out-of-Distribution Trajectories** section, with the **Spin** motion. The described phenomenon can be observed at the edges of the images with **Spin** motion, where those regions of the scene often move beyond the image boundaries before returning in the future. A qualitative example of this is shown in Figure E.1.

Conditioning on an arbitrary number of frames could theoretically solve this problem. However, the practicality of this solution is limited by the ability to design models that can process an arbitrary number of inputs, and the model’s ability to generalize to out-of-distribution camera poses (e.g., far away cameras in large scenes). Leveraging many images for generation is a potentially significant direction for future work.



(a) Initial image



(b) Image after returning close to the initial camera position.

Figure E.1: The initial frame and the final frame from a generated sequence with the *spin* motion. Notice the final frame has returned to a location similar to the initial frame, but the bottom left region on the floor has changed appearance.